ORIGINAL ARTICLE



On the depth-averaged models of ice-covered flows

Berkay Koyuncu¹ · Lahcen Akerkouch² · Trung Le^{1,2}

Received: 28 March 2024 / Accepted: 24 July 2024 © The Author(s) 2024

Abstract

Impact of ice coverage is significant in controlling the depth-averaged velocity profile and influencing morphological processes in alluvial channels. However, this impact is largely unknown under field conditions. In this work, a numerical method is introduced to compute the depth-averaged velocity profile in irregular cross-sections of ice-covered flows, based on the Shiono-Knight approach. The momentum equation is modified to account for the presence of secondary flows and the ice coverage. The equations are discretized and solved with velocity boundary conditions at the bank and at one vertical. Our approach only requires the cross-section geometry and a single velocity measurement near the highvelocity region, offering a significant advantage in inaccessible locations by avoiding the need to measure the velocity profile in the entire cross-section. The proposed model is then validated using depth-averaged velocity profile and secondary flow patterns from laboratory observations, analytical solution, and Large-Eddy Simulation. Finally, the method is applied to infer depth-averaged velocity profiles in the Red River of the North, United States, to test its performance in meandering sections. The proposed method demonstrates its robustness in reconstructing flow profiles in ice-covered conditions with a minimal amount of available data, which is crucial for assessing erosion risks and managing spring floods in cold regions.

Article Highlights

- A novel method to compute depth-averaged profile in ice-cover flows.
- The friction factor plays the most important role in the profile.
- The double-stacked vortices might exist and impact the profile's shape.

Keywords Depth-averaged profile · Ice cover · Shiono-Knight model · Secondary flow

Published online: 02 August 2024

Civil, Construction, and Environmental Engineering, North Dakota State University, 1410 North 14th Avenue, Fargo, ND 58102, USA



[☐] Trung Le trung.le@ndsu.edu

Environmental and Conservation Sciences, North Dakota State University, 1340 Administration Avenue, Fargo, ND 58102, USA

1 Introduction

In regions with freezing temperatures, ice cover is periodically observed in natural and artificial channels [20, 53, 55]. However, the effects of the frozen surface on flow dynamics remain poorly understood [11, 48, 50], particularly in alluvial streams [12]. Previous studies [30, 32] suggest that the frozen surface acts as an additional boundary roughness and leads to an increase in flow complexity by facilitating the interaction between the flow and the channel's bed. The resulting dynamics lead to changes in the three-dimensional flow structures, which might have important consequences in alluvial processes [54]. The duration of coverage of river ice has recently been reported to decrease in the Northern Hemisphere [57] due to the impacts of climate change. Hence, studying flow dynamics in ice-covered channels will address the gap in knowledge of river flows in cold regions, which have been mostly studied under open-surface conditions.

On the contrary to the open-surface condition, the vertical velocity profile follows a two-layer structure (two-layer hypothesis) [13, 27] in ice-covered flows: (1) the upper ice layer, and (2) the lower bed layer [53, 59]. These layers are separated by the zero shear stress plane [27, 34]. In practice, the maximum velocity plane was also shown to be close to the separation plane [13, 25, 48] and thus it could also be used to monitor the separation of these layers as well. The location of the maximum velocity plane is sensitive to the ice and bed roughness and it generally tends to approach the smoother boundary [47]. A correct distribution of resistance accurately divides the water column into layers as Einstein's treatment method [9] suggests, moreover, the average velocity of all sections is assumed to be equal to the depth-averaged velocity of the water column. Hence, a comprehensive roughness analysis is a key factor in computing velocity profiles [26, 59].

Estimating the depth-averaged velocity in ice-covered flows is crucial for many hydraulic applications [44, 48, 58]. Depth-averaged velocity is influenced by various factors [45], including ice cover properties, channel geometry, and flow discharge. Laboratory experiments [16, 48, 51, 53] are generally used to estimate the impacts of these factors on the depth-averaged velocity profiles. While these laboratory efforts provide the basic knowledge of hydraulic engineering applications [59], depth-averaged profiles at field scales have not been examined in detail [22, 23, 30, 32]. The analytical framework to study depth-averaged profile and its dependence on the secondary flow patterns are discussed below.

1.1 Shiono-Knight model for ice-covered flows

One of the most popular methods for computing the depth-averaged velocity is the Shiono-Knight model (SKM) [42], which was developed based on the two-dimensional Reynolds Averaged Navier-Stokes (RANS) equations [37] for a straight channel with fully-developed turbulent flows. The SKM was later improved by Shiono and Knight [43] with the integration of secondary currents coefficient (*K*) and adapted for curved channels [46].

The RANS equations can be combined and reduced to [43]:

$$\rho \left[\frac{\partial UV}{\partial y} + \frac{\partial UW}{\partial z} \right] = \rho g S_0 + \frac{\partial \tau_{yx}}{\partial y} + \frac{\partial \tau_{zx}}{\partial z}$$
 (1)

where ρ is the water density; U, V, and W are the time-averaged velocity components in x (streamwise), y (lateral/transverse), and z (vertical) directions, respectively; τ_{yx} and τ_{zx} are



the Reynolds shear stresses with respect to the horizontal and vertical planes, respectively. The above momentum equation can be solved analytically for the depth-averaged profile $U_d(y) = \frac{1}{H} \int_0^H U(y) dz$ if the shape of the cross-section is precisely known.

In ice-covered channels, Wang et al [53] suggests that Eq. 1 can be integrated along the depth (H) as:

$$\rho \frac{\partial (H(UV)_d)}{\partial y} = \rho g H S_0 + \frac{\partial (H\overline{\tau}_{yx})}{\partial y} - \chi_d \tau_d \tag{2}$$

It is required that the resistance of the ice layer is reflected by the parameter χ_d , which is the total dimensionless wetted perimeter of the river bed (χ_b) and the ice cover (χ_i) per unit width $(\chi_d = \chi_b + \chi_i)$; $\overline{\tau_{yx}}$ and τ_d are the depth-averaged transverse and bed Reynolds shear stresses; g is the gravitational acceleration. S_0 is the channel bed slope. The term χ_d is used to calculate comprehensive hydraulic radius $(R_d = A_d/\chi_d)$ for ice-covered conditions. It has a critical role in the estimation of combined friction factor (f_d) of channel bed and ice cover.

Application of eddy viscosity assumption generally leads this term to be expressed as follows:

$$\overline{\tau_{yx}} = \rho \overline{\epsilon_{yx}} \frac{\partial U_d}{\partial y} \tag{3}$$

where $\overline{\epsilon_{yx}}$ is the depth-averaged eddy viscosity. Invoking the definition of the bed shear stress and the eddy viscosity assumption, we have:

$$\begin{split} \overline{\epsilon_{yx}} &= \lambda_d u^* H = \lambda_d H U_d \sqrt{\frac{f_d}{8}} \\ \tau_d &= C_f \rho U_d^2 = \rho U_d^2 \frac{f_d}{8} \end{split} \tag{4}$$

 C_f and f_d are the drag coefficient and the comprehensive Darcy-Weisbach friction factor, respectively. λ_d is the dimensionless eddy viscosity; u^* is the shear velocity; τ_d is the comprehensive shear stress. The impact of the secondary flow was introduced to this relationship [10, 53] as the secondary flow coefficient (K) [10]: $(UV)_d = KU_d^2$. Hence, the depth-averaged form of the governing equation can be derived as follows:

$$\rho g H S_0 - \rho \frac{f_d}{8} \chi_d U_d^2 + \frac{\partial}{\partial y} \left(\rho \lambda_d H^2 \sqrt{\frac{f_d}{8}} U_d \frac{\partial U_d}{\partial y} \right) = \frac{\partial (\rho H K U_d^2)}{\partial y} \tag{5}$$

This equation can be solved analytically to estimate U_d in special cases as discussed below.

1.2 Analytical solution for Shiono-Knight equations

For symmetrically trapezoidal channels (see Fig. 1b), Wang et al [53] proposes that Eq. 5 can be solved analytically by dividing the cross-section into three distinct zones with known side slopes (1:s): (1) flood plain $(s = \infty)$; (2) the side slope (s = 1); and (3) the main channel $(s = \infty)$. It is required that wall boundary conditions are applied on both sides of the channel (y = 0) and y = B = 1 m) as U(y = 0) = 0 and U(y = B = 1 m) = 0. As the channel geometry is symmetrical with the total width of B, the mid-boundary condition



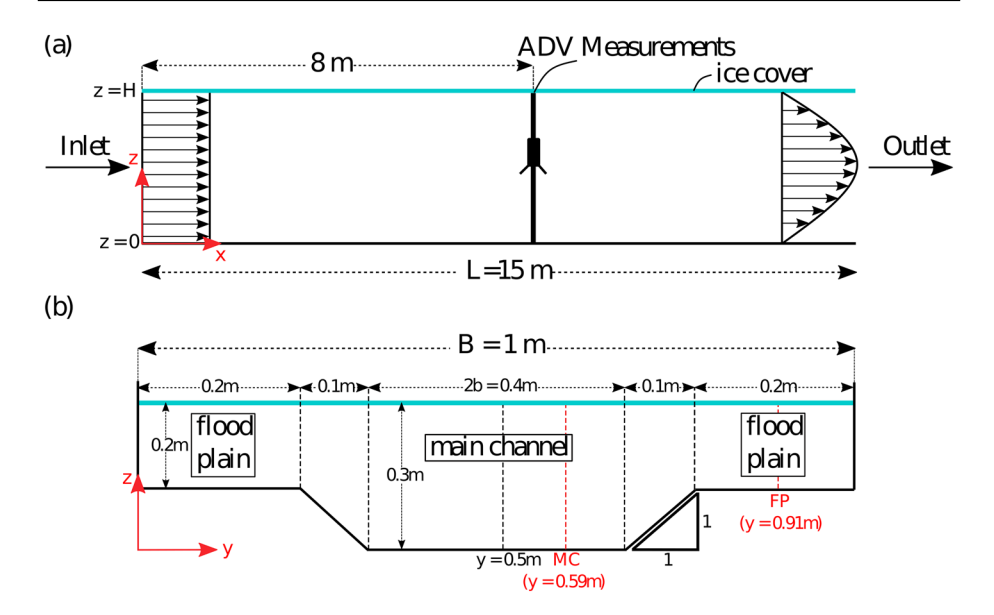


Fig. 1 Dimensions of the laboratory flume in Wang et al [53]. **a** The side view of the flume shows the location of the measured plane. The domain length L = 15m; **b** the cross-sectional sketch shows the locations of the measured data in the main channel (MC) and the floodplain (FP) verticals. The channel center is represented with a black dash line at y = 0.5 m. Here, b and H are the semi-width of the cross-section and the flow depth, respectively

is needed $(y = \frac{B}{2})$ where the maximum velocity U_{max} occurs. Using these boundary conditions, Eq. 5 can be solved for one-half of the channel's cross-section.

 U_d is computed for the main channel and the flood plain (constant flow depth- $s=\infty$) using:

$$U_d = \sqrt{C_1 e^{r_1 \left(y - \frac{B}{2}\right)} + C_2 e^{r_2 \left(y - \frac{B}{2}\right)} + \omega}$$
 (6)

where r_1 , r_2 , and ω are the coefficients; and C_1 and C_2 are the case-specific unknown constants. The values of C_1 and C_2 are not known in advance and must be calculated by fitting to the observational data. Other coefficients can be calculated as:

$$r_{1} = \frac{1}{\lambda_{d}H} \left(\frac{8}{f_{d}}\right)^{1/2} \left(K + \sqrt{K^{2} + 2\lambda_{d}\chi_{d} \left(\frac{f_{d}}{8}\right)^{3/2}}\right)$$

$$r_{2} = \frac{2K}{\lambda_{d}H} \left(\frac{8}{f_{d}}\right)^{1/2} - r_{1}$$

$$\omega = \frac{8gHS_{0}}{f_{d}\chi_{d}}$$

$$(7)$$

For s = 1 (side slopes), the analytical solution for U_d is given as:

$$U_d = \sqrt{C_3 \xi^{\alpha_1} + C_4 \xi^{\alpha_2} + \mathcal{A}\xi} \tag{8}$$



where C_3 and C_4 are the unknown constants that depend on the case setup; ξ presents the local flow depth on the side slope length of the trapezoid ($\xi = H - (y - \frac{B}{2} - b)/s$). Here, b is the semi-width of the main channel (see Fig. 1). The coefficients (α_1 , α_2 , and \mathcal{A}) of this equation are calculated as:

$$\alpha_{1} = \frac{\mathcal{L} - M + \sqrt{(M - \mathcal{L})^{2} - 4N\mathcal{L}}}{2\mathcal{L}}$$

$$\alpha_{2} = \frac{\mathcal{L} - M - \sqrt{(M - \mathcal{L})^{2} - 4N\mathcal{L}}}{2\mathcal{L}}$$

$$\mathcal{A} = -\frac{gS_{0}}{\frac{\lambda_{d}}{s^{2}} \left(\frac{f_{d}}{8}\right)^{1/2} + \frac{2K}{s} - \frac{f_{d}}{8}\chi_{d}}$$
(9)

The parameters
$$\mathcal{L}$$
, M , and N are calculated as: $\mathcal{L} = \frac{\lambda_d}{2 s^2} \left(\frac{f_d}{8}\right)^{1/2}$, $M = \frac{\lambda_d}{2 s^2} \left(\frac{f_d}{8}\right)^{1/2} + \frac{K}{s}$, $N = \frac{K}{s} - \frac{f_d}{8} \chi_d$.

As shown above, the analytical solution is only available if the side slope s is a constant value [59]. Therefore, it is not possible to apply this analytical method to compute U_d with arbitrary cross-sections.

1.3 The need to compute U_d for alluvial channels

The need to estimate U_d in field conditions has led to the use of one-dimensional [29, 40] or two-dimensional [31, 41] models to capture large-scale hydrodynamic patterns in rivers. These models [4, 21, 29] are computationally expedient and can incorporate large-scale hydro-climatic condition easily [38]. However, they cannot provide details on the turbulent characteristics [31] in a cross-section. Recent advancements in Computational Fluid Dynamics (CFD) have enabled three-dimensional modeling of river flows [28, 52]. These CFD models use advanced turbulence models such as large-eddy simulation (LES) and Reynolds-averaged Navier–Stokes (RANS) equations [19]. To date, LES was mostly performed under open-surface condition [28].

Natural rivers and streams feature irregular cross-sectional shapes [7], which prohibit the use of analytical solution such as Eq. 6 and 8 for ice-covered flows. It is necessary to develop and validate a general method for computing depth-averaged flows in arbitrary cross-section. This study aims to develop such a general method using numerical approximation. The main objectives are:

- Develop a procedure to compute depth-averaged profile U_d (a numerical solution to Eq. 1) in compound channels with arbitrary geometries.
- Validate the proposed numerical procedure with laboratory, analytical solution, and field data.
- Identify the key factors regulating the profile, especially the impact of secondary flows
- Investigate the sensitivity of the U_d solution to the governing parameters $(f_d, \lambda_d, \text{ and } K)$.

First, a numerical procedure to determine U_d is developed for compound channels using the SKM-based method of [53]. Second, Large Eddy Simulation (LES) is also performed and compared with experimental data in a straight channel in the experiment of Wang et al [53]



to provide a complete three-dimensional flow field to serve as the validation data. Third, the proposed numerical procedure is validated using the available data of experiments of Wang et al [53] and the obtained LES results. Finally, the validated procedure is used to investigate the range of the governing parameters (f_d , λ_d , and K) in a river reach of the Red River of the North, United States to examine its applicability for field conditions.

2 Methodology

2.1 Laboratory data

The experimental setup for ice-covered flows is performed by Wang et al [53]. The experiment is performed on a $L_0 = 12 m \log (x \text{-streamwise})$, B = 1 m (y -lateral), and the total depth H = 0.3 m (z -depth) in a straight/trapezoidal flume (Fig. 1a) with fully-covered condition (see Fig. 1b).

A whole foam piece is used to mimic the full coverage of the ice layer. The channel bed slope was $S_0 = 0.01\%$ and the side slope (s:1) of the trapezoid was s=1. The flow depth is 0.3 m and 0.2 m on the main channel and the flood plain, respectively. The flow discharge is $Q = 0.0510 \, m^3/s$. The monitoring cross-section is chosen at a distance of 8 m from the inlet as shown in Fig. 1a. As the channel is symmetrical, flow measurements (Acoustic Doppler Velocimetry) are only obtained starting from the channel center and towards the right wall along the cross-stream direction $(y \ge 0.5m)$.

In the experiments of Wang et al [53], the roughness length of the surface cover (foam - k_{si}) and channel bed (organic glass - k_{sb}) are not reported. As these roughness values are important for velocity profiles, the logarithmic fitting [35] is used to determine their values as follows:

$$\frac{U(z)}{u_{\star}} = \frac{1}{\kappa} \ln \frac{z}{k_s} + 8.5$$

$$u^{\star} = \kappa m$$

$$k_s = \exp\left[8.5\kappa - \frac{\gamma}{m}\right]$$
(10)

where U(z) is the local streamwise velocity at depth z (0 < z < H); κ is the Von Karman constant (0.39 < κ < 0.41) [3, 33, 35, 36]; k_s is the roughness length of the surface; u^* is the shear velocity of the surface (either the bed (u_b^*) or the ice (u_i^*)); and γ and m are the intercept point and the slope of the best-fit regression line, respectively.

Since the vertical velocity profiles are measured on the flood plain (FP) and the main channel (MC) separately by Wang et al [53], the roughness lengths $(k_{si} \text{ and } k_{sb})$ can be estimated by fitting Eq. 10 to find the appropriate values of m, and γ . As seen in Table 1, the fitting method yields relatively similar values for the bed k_{sb} ($\approx 0.00535 \, m$). However, different values k_{si} are found in the FP and MC regions $k_{si} = 0.00026 - 0.00091 \, m$. It is thus necessary to investigate the impact of k_{si} on the flow profile. The values of the roughness length are used as inputs for the Large Eddy Simulations as described below.



2.2 Large Eddy Simulation (LES) of flows in the trapezoidal channel

A series of LES is carried out to determine the three-dimensional flow structure in the trapezoidal channel (Fig. 1). The open-source code Virtual Flow Simulator (VFS) is used to simulate the turbulent flows to replicate the experimental configuration of Wang et al [53]. The VFS code has been validated with laboratory experiments under both fixed bed and live bed cases [17, 18]. The numerical code has exhibited its efficiency and accuracy in capturing flow dynamics in open-surface conditions Khosronejad et al [17], Kang et al [15], Kang and Sotiropoulos [14]. In this context, we only provide a concise overview of the adopted numerical techniques.

The filtered incompressible Navier–Stokes equations are solved using a fractional step method in a structured grid domain. The momentum equation is tackled using an implicit approach with a matrix-free Newton-Krylov solver [5]. The Poisson equation is solved using FGMRES with multi-grid preconditioner with Petsc numerical library [14, 15, 28]. The channel surface is represented as an immersed surface inside the computational domain [14]. The wall boundary condition is then reconstructed at the immersed nodes using the roughness length k_s . For the details of the numerical methods, the reader is encouraged to review our previous works [14, 18, 28].

To examine the impacts of the roughness length k_s on the flow profiles, numerical simulations are performed using different roughness lengths. Initially, the bed (glass) roughness and the foam (ice) roughness are set to be $k_{sb}=0.00535~m$ and $k_{si}=0.00059~m$, respectively. These values are chosen as the averaged roughness of glass (bed) and foam (ice) in Table 1. Subsequently, the values of k_{si} and k_{sb} are systematically varied as $k_{sb}=0.00535~m-0.00600~m$ and $k_{si}=0.00059~m-0.00800~m$. The computational grid is a structured grid, which is from 1.3M (Grid-1) to 10.0M (Grid-3) as shown in Table 2. The grid spacing (Δ) is chosen to be fine enough so that the assumption on the logarithmic law of the wall is valid at the immersed node ($\Delta^+ = \frac{\Delta u^*}{v} \le 1000$). Here v is the fluid viscosity. The combination of the computational grid, k_{si} , and k_{sb} gives rise to a total of 5 simulation cases as shown in Table 3.

While the flow rate is set exactly as in the experimental value of $Q=0.0510~m^3/s$, the flow profile is not reported [53]. Therefore, a uniform flow is assumed at the inlet (see Fig. 1) with the bulk velocity $\overline{U}=0.204~m/s$. At the outlet, a fully developed flow condition is assumed. The flow-through time is defined as $T_0=\frac{L}{U}$. Due to the uncertainty in the inlet flow profile, the length of the simulation domain L=15~m is made slightly longer in comparison to the actual channel length L_0 to accommodate the growth of the boundary layer along the computational domain. In all cases, the simulation is first run for a period of $20T_0$ to initiate the turbulent flow along the domain length (L). The time-averaged flow field is then acquired by accumulating the results starting from $t=20T_0$ to $t=40T_0$. The turbulent statistics are computed from the accumulated data.

2.3 Field measurement

Field surveys during the winter season of 2021 are conducted in a bend of the Red River of the North near Lindenwood Park, Fargo, North Dakota, United States (see Fig. 2). The channel bed of the Red River is mostly identified as clay and silt [56].

The Acoustic Doppler Current Profiler (ADCP), Sontek M9, is used to monitor velocity components at each vertical under the SmartPulse mode of 1 *MHz* as seen in Fig. 2a. The reliability of the data sets is confirmed by monitoring the beam separation (signal-to-noise





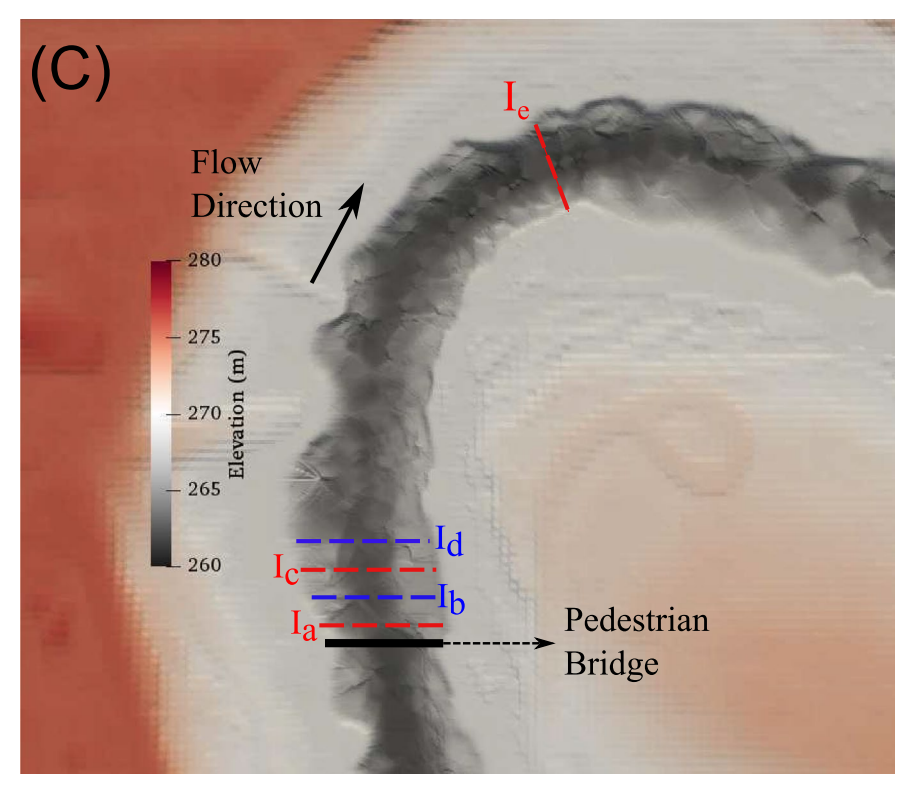


Fig. 2 Acoustic Doppler Current Profiler measurement and the locations of the cross-sections in the study area. **A** The measurement instruments; **B** Opening ice holes in the cross-sections; **C** The locations of the cross-sections I_a , I_b , I_c , and I_d , in the river reach of the Red River of the North (North Dakota, United States). The Digital Terrain Model is generated from the LiDAR data (North Dakota Water Commission - https://lidar.dwr.nd.gov/ and the surveyed bathymetry data



ratio - SNR) of all measurements during and after the acquisitions. To place the sensor below the ice cover, a gas auger is used to open ice holes large enough to lower the M9 into the flows as depicted in Fig. 2b. In each cross-section, the distance from the left bank (the reference point) ℓ is noted for each ice hole (vertical). The measurement period in each ice hole was limited to 120 s due to the impact of low air temperature on our equipment. The details of the number of ice holes in each cross-section are summarized in Table 4 and Fig. 2c. Five separate cross-sections are surveyed: I_a (Feb/19/21), I_b (Feb/20/21), I_c (Feb/21/2021), I_d (Feb/21/2021), and I_e (Feb/21/2021). Among these cross-sections, I_a through I_d are separated by 6 m spacing between each other. The cross-section I_e is located right after the bend apex, approximately 310 m away from I_a .

The cross-sections and the ice hole locations are shown in Fig. 3. The wet area of the cross-sections and the wetted perimeter are approximated as $A \approx 120 \, m^2$ and $P \approx 95 \, m$, respectively. The details of the field campaigns and the data processing can be found in our previous work [23, 24].

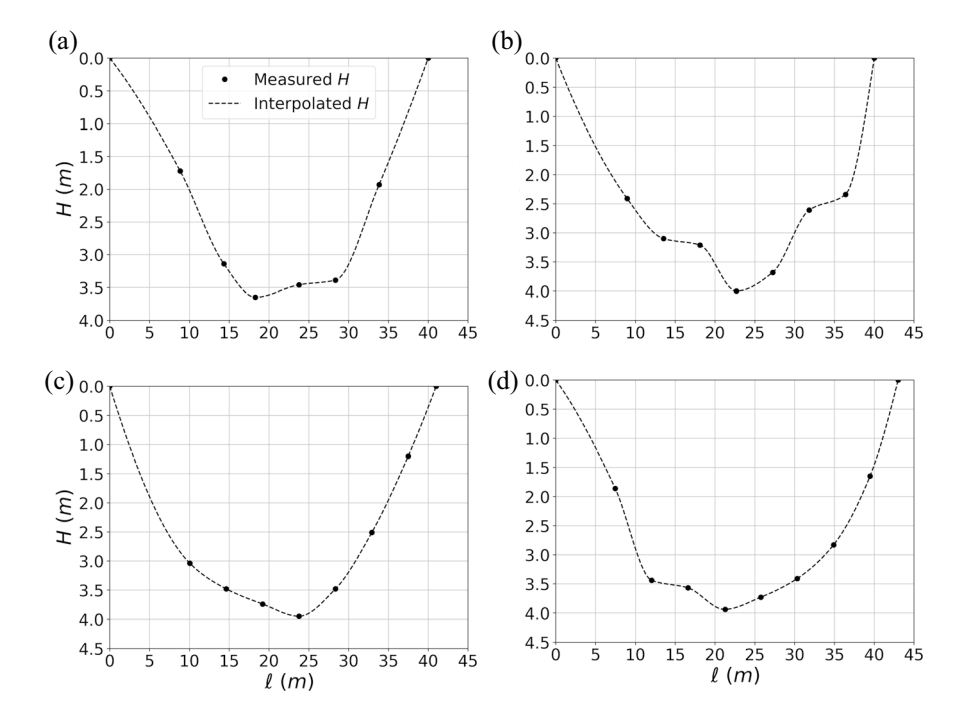


Fig. 3 The measured flow depth (H) in each ice hole and the reconstructed shapes of the cross-sections using the Piecewise Cubic Hermite Interpolating Polynomial (PCHIP) function for $\mathbf{a}\ I_a$, $\mathbf{b}\ I_b$, $\mathbf{c}\ I_c$, and $\mathbf{d}\ I_d$. The details of the measurements are shown in Table 4



3 SKM-based numerical solution for depth-averaged profile in an arbitrary cross-section

3.1 Numerical procedure

In this section, a novel algorithm is proposed to solve the momentum equation of the SKM in arbitrary cross-sections. Specifically, the numerical approximation of Eq. 5 can be explained as follows.

$$\rho g H S_0 - \rho \frac{f_d}{8} \chi_d U_d^2 + \rho \lambda_d \sqrt{\frac{f_d}{8}} \frac{\partial}{\partial y} \left(H^2 \frac{\partial (U_d^2)}{\partial y} \right) = \rho K \frac{\partial (H U_d^2)}{\partial y}$$
 (11)

For the tidiness of operations, a notation arrangement is made at this point as $\mathcal{V} = U_d^2$. Following the distribution of derivatives and applying the product rule, the momentum equation becomes:

$$\rho g H S_0 - \rho \frac{f_d}{8} \chi_d \mathcal{V} + \rho \lambda_d \sqrt{\frac{f_d}{8}} \left(\frac{\partial H^2}{\partial y} \frac{\partial \mathcal{V}}{\partial y} + H^2 \frac{\partial^2 \mathcal{V}}{\partial y^2} \right) = \rho K \left(\frac{\partial H}{\partial y} \mathcal{V} + H \frac{\partial \mathcal{V}}{\partial y} \right)$$
(12)

Afterward, three-point central differencing (2^{nd} order accurate) is applied for all derivatives assuming a constant spacing between two successive ice holes i - 1, i, and i + 1 (spacing Δy).

$$\rho g H_{i} S_{0} - \rho \frac{f_{d}}{8} \chi_{d} \mathcal{V} + \rho \lambda_{d} \sqrt{\frac{f_{d}}{8}} \left(2H_{i} \frac{H_{i+1} - H_{i-1}}{2\Delta y} \frac{\mathcal{V}_{i+1} - \mathcal{V}_{i-1}}{2\Delta y} + H^{2} \frac{\mathcal{V}_{i+1} - 2\mathcal{V}_{i} + \mathcal{V}_{i-1}}{\Delta y^{2}} \right) \\
= \rho K \left(\mathcal{V}_{i} \frac{H_{i+1} - H_{i-1}}{2\Delta y} + H_{i} \frac{\mathcal{V}_{i+1} - \mathcal{V}_{i-1}}{2\Delta y} \right) \tag{13}$$

$$-\rho \frac{f_{d}}{8} \chi_{d} \mathcal{V} + \rho \lambda_{d} \sqrt{\frac{f_{d}}{8}} \left(2H_{i} \frac{H_{i+1} - H_{i-1}}{2\Delta y} \frac{\mathcal{V}_{i+1} - \mathcal{V}_{i-1}}{2\Delta y} + H^{2} \frac{\mathcal{V}_{i+1} - 2\mathcal{V}_{i} + \mathcal{V}_{i-1}}{\Delta y^{2}} \right) - \rho K \left(\mathcal{V}_{i} \frac{H_{i+1} - H_{i-1}}{2\Delta y} + H_{i} \frac{\mathcal{V}_{i+1} - \mathcal{V}_{i-1}}{2\Delta y} \right) = -\rho g H_{i} S_{0}$$
(14)

Here, terms are grouped for the values of V at three successive ice holes (i-1, i, and i+1) as follows:

$$A_{i} = -\rho \lambda_{d} \sqrt{\frac{f_{d}}{8}} 2H_{i} \frac{H_{i+1} - H_{i-1}}{4\Delta y^{2}} + \rho \lambda_{d} \sqrt{\frac{f_{d}}{8}} \frac{H_{i}^{2}}{\Delta y^{2}} + \rho K \frac{H_{i}}{2\Delta y}$$

$$B_{i} = -\rho \frac{f_{d}}{8} \chi_{d} - \rho \lambda_{d} \sqrt{\frac{f_{d}}{8}} \frac{2H_{i}^{2}}{\Delta y^{2}} - \rho K \frac{H_{i+1} - H_{i-1}}{2\Delta y}$$

$$C_{i} = \rho \lambda_{d} \sqrt{\frac{f_{d}}{8}} \left(2H_{i} \frac{H_{i+1} - H_{i-1}}{4\Delta y^{2}} \right) + \rho \lambda_{d} \sqrt{\frac{f_{d}}{8}} \frac{H_{i}^{2}}{\Delta y^{2}} - \rho K \frac{H_{i}}{2\Delta y}$$

$$D_{i} = -\rho g H_{i} S_{0}$$
(15)

We now need to solve the system of equations i = 1 ... N (N is the number of ice holes) to find V_i as:



$$A_i \times \mathcal{V}_{i-1} + B_i \times \mathcal{V}_i + C_i \times \mathcal{V}_{i+1} = D_i$$
(16)

An in-house Matlab script is developed to invert this linear system of equations to find the depth-averaged velocity at each ice hole i^{th} ($U_d^i = \sqrt{V_i}$). Note that the coefficients A_i , B_i , C_i , and D_i can be determined before ice measurements if the local bathymetry, the ice coverage, and the bed roughness are known. However, it is required to supply the boundary conditions (e.g. known values of U_d at certain locations) to solve Eq. 16 numerically.

3.2 Application considerations

As the natural cross-sections are not symmetrical as in the experimental settings by Wang et al [53], it is not possible to consider only one-half of the channel. In this case, it is required to reconsider the mid-boundary location that divides the cross-section into two separate parts with the number of ice holes as N_1 and N_2 so that Eq. 16 can be solved correspondingly for each part. In other words, one value of $U_d^{mid-boundary}$ must be known at one ice hole around the middle part of the channel (i = mid - boundary), which is classified as the mid-boundary condition. There is also a need to prescribe the values of $U_d = 0$ at the left bank (i = 0) and the right bank (i = N). Note that there is no certain requirement on the location of such an ice hole mid - boundary because Eq. 16 only requires that U_d must be known for the beginning and end points of the part. The steps for our numerical procedure are as follows:

- Step 1: Measure the depth-averaged velocity and depth at each ice hole from the ADCP data.
- Step 2: Build the shape of the cross-section. To be as practical as possible, we assume that the cross-section is not surveyed in advance and is only known via measurements at the limited number of ice holes. To reconstruct the shape of the cross-section from the depth measurements at each ice hole. The entire shape of each cross-section is reconstructed using the Piecewise Cubic Hermite Interpolating Polynomial (PCHIP) method from the flow depth in each ice hole.
- Step 3: Select a number of verticals for computations (N). Theoretically, the larger the number of N, the obtained numerical values U_d^i will be more accurate.
- Step 4: Decide the mid boundary condition U_d^{mid-boundary} by selecting the ice hole mid boundary. The left (outer bank) and right (inner bank) parts are completely separated by the mid boundary ice hole.
- Step 5: Solve Eq. 16 separately for the left and right parts by splitting the number of ice holes into $N = N^L + N^R 1$. Here N_L and N_R are the number of verticals in the left and right parts, respectively. Please note that Eq. 16 solves both sides independently. Therefore, the choice of N_L and N_R can be varied.



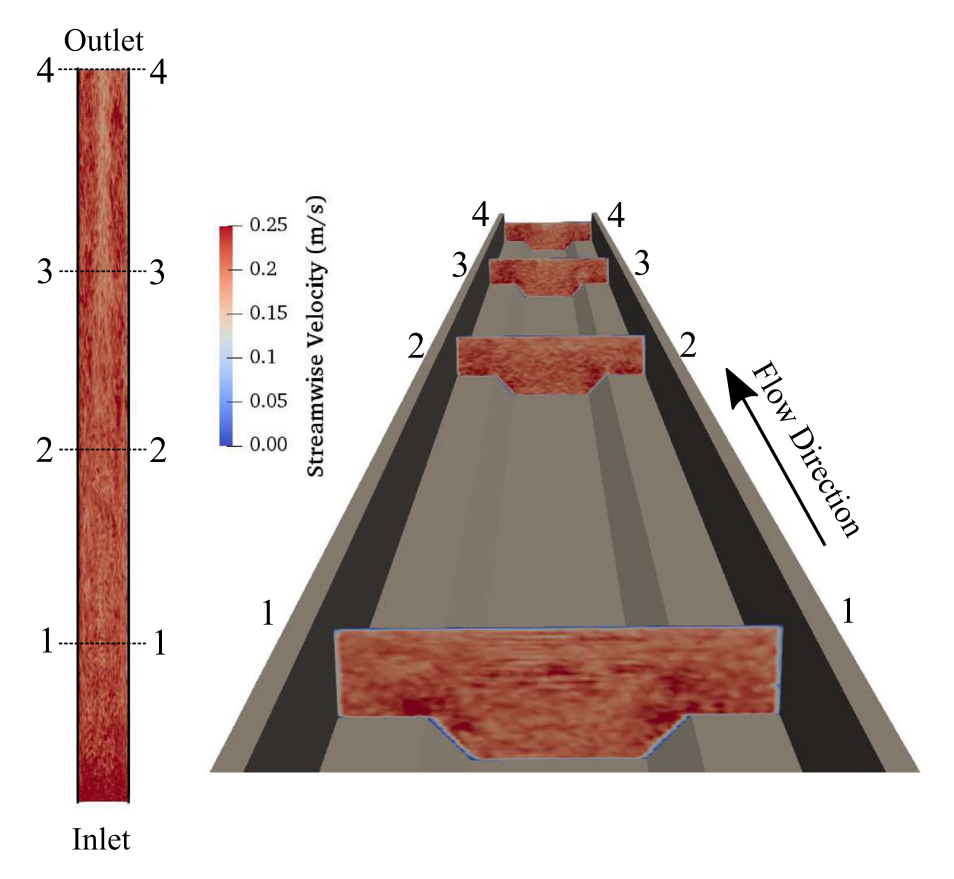


Fig. 4 A planform (left) and cross-sectional view (right) of the Large Eddy Simulation setup. Cross-sections 1, 2, 3, and 4 are separated with an equal spacing of 3.75 *m*. The cross-section 4 corresponds to the outlet plane

• Step 6: Compare the obtained values of U_d^i with the measured data from ADCP.

4 Result

4.1 Three-dimensional flow structures in the trapezoidal channel

The flow dynamics in the trapezoidal channel are reconstructed from the Large Eddy Simulation results as shown in Fig. 4. The changes in the depth-averaged flow profile are monitored along the computational domain in the cross-sections 1, 2, 3, and 4. As there are uncertainties in the value of roughness (k_{si} and k_{sb}) and the inlet flow condition, it is necessary to identify the impacts of these uncertainties to the LES results by comparing the computational results with the experimental data.

The impact of roughness on the vertical profile of streamwise component (U(z)) is investigated by comparing the simulation results of Cases 1, 2, and 3 (Table 3) using the same computational Grid-1. As shown in Fig. 5, the main channel and floodplain verticals



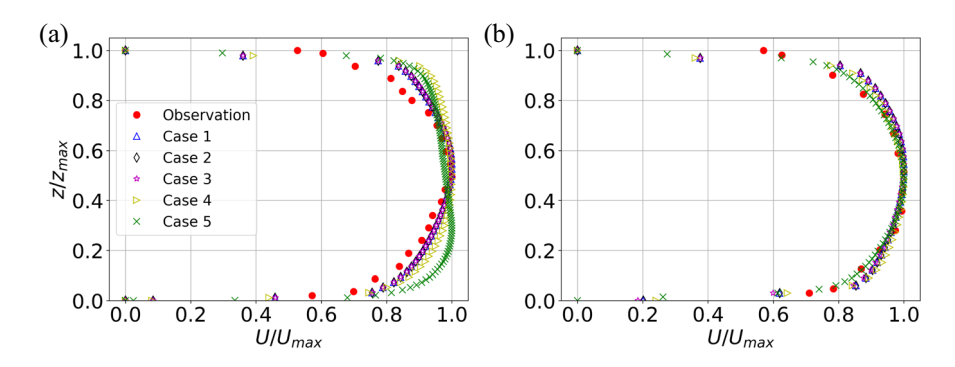


Fig. 5 The observed and computed (LES) vertical velocity profiles for **a** the main channel vertical (MC, $y = 0.59 \, m$), and (b) for the floodplain vertical (FP, $y = 0.91 \, m$) at cross-section 4. The exact locations of these verticals are shown in Fig. 1. The grid computational setups are shown in Tables 2 and 3

Table 1 The fitted values of k_s for foam (ice) and glass (bed) in the main channel (MC) and floodplain (FP) verticals using the experimental data of Wang et al [53]

Material	Roughness length, k_s (m)
Foam (from MC)	0.00091
Foam (from FP)	0.00026
Glass (from MC)	0.00490
Glass (from FP)	0.00570

Table 2 Computational grids for the trapezoidal channel of [53]. The value of Δ_{max}^+ is estimated using $(\Delta^+)_{max} = \frac{max(\Delta x, \Delta y, \Delta z)u_{\star}}{v}$. The shear velocity is $u^{\star} \approx 0.0054 \, m/s$, which is estimated from the measured profile of Wang et al [53]

Grid name	Size	$\Delta x(m)$	$\Delta y(m)$	$\Delta z(m)$	$(\Delta^+)_{max}$
Grid-1	$251 \times 101 \times 51$	0.0598	0.0099	0.0059	322
Grid-2	$1001 \times 101 \times 51$	0.0150	0.0099	0.0059	81
Grid-3	$1001\times101\times101$	0.0150	0.0099	0.0030	81

are 0.3 m and 0.2 m deep (see also Fig. 1), respectively. Although the values of k_{si} and k_{sb} are varied significantly, the vertical profiles in the main channel and the floodplain remain nearly identical. Thus, the LES results show that the roughness lengths of the ice and the bed does not impact the U(z) significantly in this experimental setup.

The sensitivity of the LES results with the computational grid is shown by comparing results of Case 1 (1.3M) and Case 4 (5.0M) in Table 3. The comparison in Fig. 5 shows that increasing the number of grid points does affect significantly the profile in the main channel but not the floodplain one. To further examine the combined impact of the computational grid and the roughness, the vertical profiles of Case 1, 4, and 5 are compared. Note that the ice roughness in Case 5 is set to be $0.0059 \, m$, which is one order of magnitude larger than the one of Case 1. It is evident that the results of the finest grid (Grid-3) in Case 5 reflects a



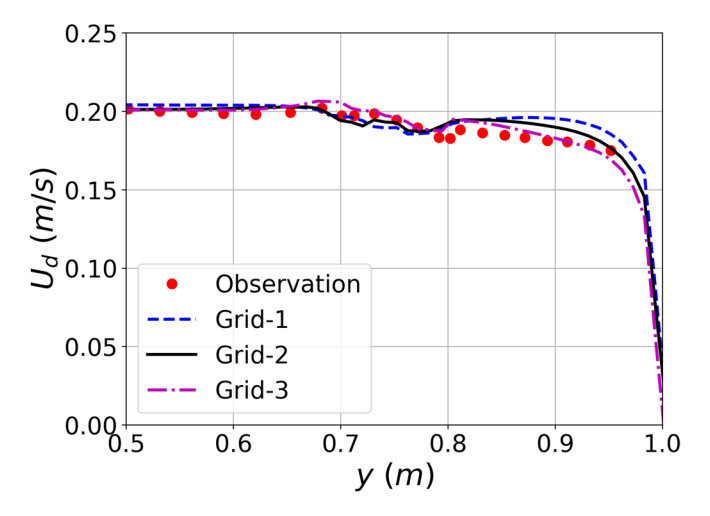


Fig. 6 Grid refinement study for the distribution of depth-averaged velocity (U_d) in Large Eddy Simulation (LES) with different grid levels (Grid-1, Grid-2, Grid-3 - see Table 2) for case 1, 4, and 5 (see Table 3), respectively at cross-section 4 (see Fig. 4). The computed profiles are also compared with the experimental observation [53], which is available only on the right side of the trapezoidal channel. The origin (y = 0.5 m) is at the center of the channel

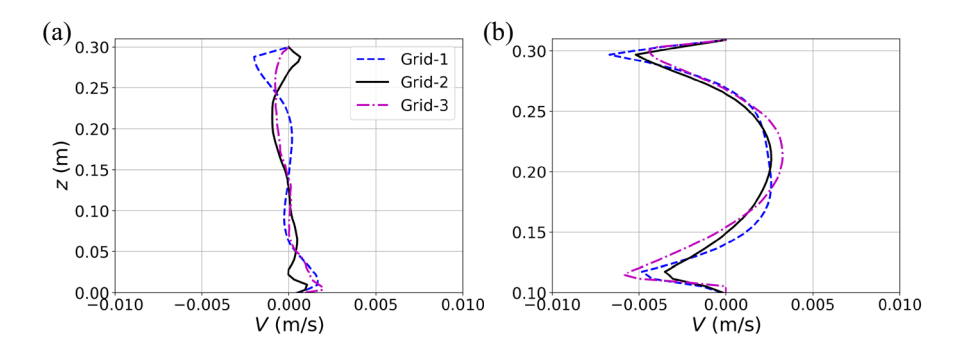


Fig. 7 The cross-stream velocity profile (V(z)) along the depth from Large Eddy Simulation under different grid levels Grid-1 (1.3M), Grid-2 (5M), and Grid-3 (10M) in cases 1, 4, and 5 (Table 2) at cross-section 4. The verticals are at $\mathbf{a} \ y = 0.59 \ m$ in the main channel, and $\mathbf{b} \ y = 0.91 \ m$ on the floodplain (see Fig. 1)

Table 3 Computational setup for simulation cases in the trapezoidal channel in Fig. 1. The combination of the computational grids (Table 2), ice roughness (k_{si}) , and bed roughness (k_{sb}) give rise to 5 simulation cases

Case	Grid	k_{si} (m)	k_{sb} (m)
1	Grid-1	0.00059	0.00535
2	Grid-1	0.00091	0.00535
3	Grid-1	0.00800	0.00600
4	Grid-2	0.00059	0.00535
5	Grid-3	0.00590	0.00535



Table 4 The summary of the hydrological data at the USGS Fargo (09020104) station and the number of ice holes in each cross-section

Case	$Q\left(m^3/s\right)$	Elevation (m)	Total verticals (ice holes)	
I_a	12.5	265.92	6	
I_b	12.8	265.92	7	
I_c	13.8	265.93	7	
I_d	13.8	265.93	8	
I_e	13.8	265.93	7	

deviation from the Case 1 and 4 data near the bed in the main channel. In brief, the vertical profile in the main channel requires the use of sufficiently fine mesh.

The depth-averaged profiles are compared across different grid levels from Grid-1 (1M), to Grid-2 (5M) and Grid-3 (10M) in Case 1, 4, and 5 as shown in Table 3. The computed velocity profiles at the cross-section 4 are then compared with the experimental observation of Wang et al [53] (see Fig. 6). The results show that the computational results generally agree with the experimental observation regardless of the uncertainties in k_{sb} and k_{si} . As the computational grid is refined, the depth-averaged profile follows closely the experimental data, especially the transition from the main channel toward the side slope. The slight decrease over the side slope is captured accurately by all the grid configurations. The result of Grid-3 agrees excellently with the experimental data, especially in the transition over the floodplain and the vicinity of the side wall (y = B = 1 m). Therefore, our grid refinement indicates that the LES is able to reproduce the depth-averaged profiles in the experiment of Wang et al [53]. Since Case 4 has the averaged values of roughness in Table 1, its simulation result is used to report the flow dynamics in the subsequent sections.

The dependence of the lateral velocity (V(z)) on the computational grid is investigated in Fig. 7 in two locations: (a) near the channel's center, and (b) on the flood plain for Case 1, 4, and 5. The results show that the value of V(z) varies largely depending on the location of the vertical. In Fig. 7a, V(z) is near zero and does not follow a particular pattern near the channel center. However, the distribution of V(z) is completely different in the floodplain vertical with three separate regions as shown in Fig. 7b. In the mid-depth region, it is skewed toward the channel wall (V > 0) whereas it is negative (V < 0) near both the ice cover and the channel bed. In this region, the numerical value of V(z) reaches $\approx 2\%$ of the \overline{U} . To investigate the dependence of V(z) on the computational grids, all profiles of V(z) are shown simultaneously on three grid configurations (Grid-1, Grid-2, and Grid-3). The computational results yield similar distributions of V(z) in both verticals. In brief, the obtained distribution of V(z) is consistent across grid resolutions. Due to the roughness values, only the computational data from Grid-2 (case 4 in Table 3) are used to report the results in the following discussions.

The secondary flow pattern in the channel is reconstructed from the LES results as displayed in Fig. 8. The secondary flow patterns of Case 4 (Table 3) are shown in Fig. 8a. Remarkably, the two-layer structure appears on the floodplain near both banks, which is consistent with the double-stacked theory. On both floodplains, two streamwise circulations are found on top of each other over the flow depth of 0.2 m. These two circulations have opposite rotational directions: (1) clockwise in the ice layer circulation, and (2) counterclockwise in the bed layer circulation. The circulations near the ice layer rotate towards



Table 5 Fitted parameters of the analytical method (Eq. 6 and 8) for each section in the trapezoidal channel (Fig. 1). Note that values of K, f_d , and λ_d are taken from Wang et al [53]. Abbreviations: Main Channel (MC), Side Slopes (SS), Floodplain (FP)

Section	f_d	λ_d	K (%)	C_1	C_2	C_3	C_4
MC	0.0280	0.067	1	-3×10^{-5}	9.9×10^{-3}	_	_
SS	0.0307	0.098	0.1	-	-	-0.143	1.5×10^{-4}
FP	0.0321	0.097	-3.5	2.5×10^{-7}	0.016	_	-

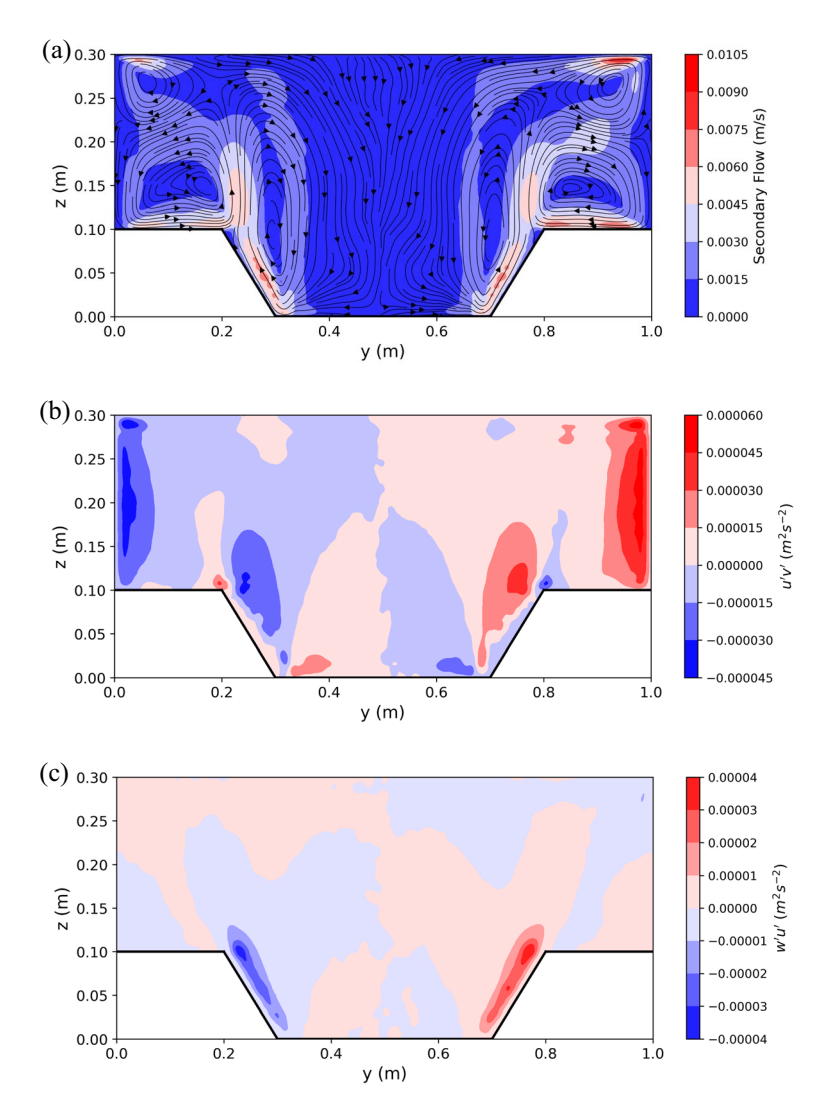


Fig. 8 Reconstruction of secondary flow patterns from Large Eddy Simulation (Case 4) at the outlet. **a** The secondary flow patterns and circulations are generated using streamlines. The cross-stream (V) and vertical (W) velocity components are used to generate the streamlines and contours. **b** Cross-sectional distribution of the turbulence statistics for $\overline{u'v'}$, and \overline{c} $\overline{u'w'}$. The area of high turbulent stresses corresponds well to the dynamics of the secondary flows

the channel center. The presence of these circulations shows the impact of rigid walls near the top (ice) and bottom (channel bed) boundaries. Interestingly, there is only one large circulation on the side slope $(0.7 \ m \le y \le 0.8 \ m)$ due to a strong downward movement of the secondary flows near the channel bed. The maximum secondary flow is located near the channel bed (both the side slope and the floodplain). Considering the bulk velocity $(\overline{U} = 0.204 \ m/s)$, the maximum secondary flow velocity reaches to $\approx 5\%$ of \overline{U} . In conclusion, our LES results indicate a significantly strong secondary flow, which forms the double-stacked circulations on floodplains.

The distribution of turbulence statistics over one cross-section is presented in Fig. 8b, c. The turbulent stresses $(\tau_{xy} = -\rho \overline{u'v'})$ and $\tau_{zx} = -\rho \overline{u'w'}$ are highly correlated to the secondary flow dynamics on the floodplain and the side slopes as seen Fig. 8b, c. The interaction between the banks (vertical walls) and the flow is shown as the elevated magnitude of $\overline{u'v'}$ as depicted in Fig. 8b. Both components $\overline{u'w'}$ and $\overline{u'w'}$ reach their highest magnitudes on the side slope as it is the location of the strongest upward movement in the secondary flows as illustrated in Fig. 8b, c. In short, the patterns of secondary flows correlate strongly with turbulent stresses.

4.2 Validation of SKM-based solution

The analytical solution (Eq. 6 and 8) is reconstructed by fitting with the measured data using the reported values of f_d , λ_d , and K in Wang et al [53] (see Table 5). Note that the values of C_1 , C_2 , C_3 , and C_4 (Eq. 6 and 8) are not reported by Wang et al [53]. Therefore, a fitting procedure was carried out to determine the values of $(C_1, C_2$ - Eq. 6) and $(C_3, C_4$ - Eq. 8) in both the main channel/floodplain and the side slopes, respectively as seen in

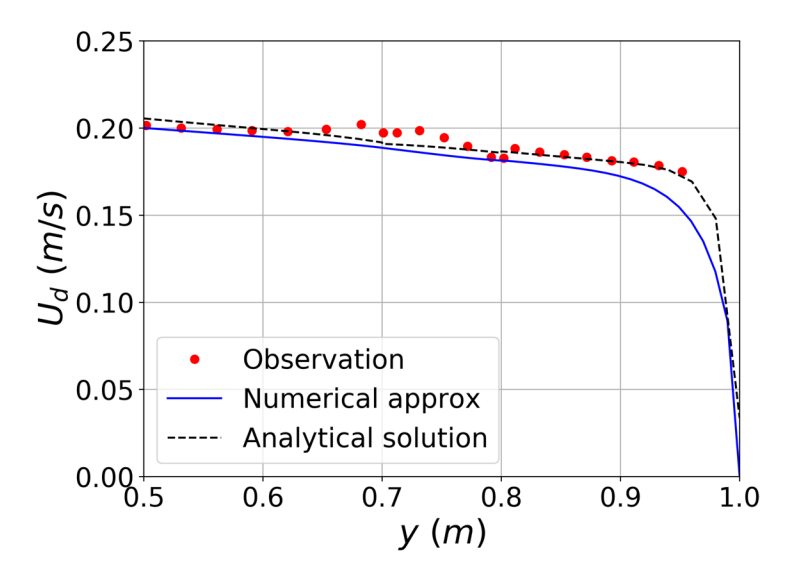


Fig. 9 Validation of numerical reconstruction (Eq. 16) for the depth-averaged velocity ($U_d(y)$) using N = 101. The numerical approximation is compared with the experimental observation of Wang et al [53], and the analytical solution (Eq. 6 and 8). The experimental data is only available on one-half (the right side) of the trapezoidal channel ($y \ge 0.5 m$)



Table 5. The obtained fitted parameters are used to generate the complete depth-averaged profile in the entire cross-section.

The comparison between the analytical solution and the measured data [53] is shown in Fig. 9. The measured U_d profile at the channel center maintains a relatively large value in the main channel $(0.5\ m \le y \le 0.7\ m)$ and only decreases as the side slope starts $(y \ge 0.7\ m)$. As the side slope of the trapezoid begins $(y = 0.7\ m)$, the measured value of U_d decreases until the slope ends $(y = 0.8\ m)$. U_d slightly increases at the transition from the slope to the floodplain at $y = 0.8\ m$. It becomes constant again in the floodplain. U_d continues to decrease sharply as near the vertical walls $(y = 1\ m$ and $U_d = 0)$. The analytical solution fails to capture the flat profile in the main channel region as well as the slight increase at $y = 0.3\ m$ as seen in Fig. 9. Note that the analytical solution is specifically available for a region with a constant slope, using either Eq. 6 $(s = \infty)$ or Eq. 8 (s = 1), the analytical profile cannot be applied for a region with non-constant slope.

The value of U_d using our numerical procedure (blue solid line - Eq. 16) is now validated with the measured data and the analytical solution as shown in Fig. 9. In this case, the mid-boundary location is chosen as the channel's center exactly as required by the numerical procedure in section 2. Although the channel geometry varies largely from $s=\infty$ in the main channel and floodplain, to s=1 on the side slope, our numerical approximation is able to compute U_d with any value of s, eliminating the need for switching the form of solution. Our results in Fig. 9 show that the numerical approximation of U_d agrees well with the measured data based only on the reported values of the governing parameters: λ_d , f_d , and K. In conclusion, our numerical solution agrees well with both the measured data and the analytical solution without the need to introduce additional parameters in the trapezoidal channel.

4.3 Application for field data

4.3.1 Range of parameters

Three parameters (K, f_d) , and λ_d are required for the SKM-based approximation, such parameters must be evaluated before applying Eq. 16 for field conditions. Although the study of Wang et al [53] provided reference values in laboratory environment, the ranges of these parameters field conditions have not been reported for ice-covered flows before. Thus, a systematic investigation of these ranges is needed as explained below.

The magnitude of K is varied in the range of 0.001 to 0.1 as suggested by previous works for both experimental data [53] and field condition [10]. Note that the value of K is typically $0.005 \le K \le 0.05$ in meandering rivers [8, 10].

The friction factor (f_d) can be estimated as Wang et al [53]:

$$f_d = \frac{8g}{\chi_b + \chi_i} \left[\frac{n_b^{3/2} + \beta n_i^{3/2}}{(1+\beta)R} \right]^{1/3} (\chi_b n_b^{3/2} + \chi_i n_i^{3/2})$$
 (17)

where R is the hydraulic radius of the bed and ice layer (R = A/P); n_b and n_i are Manning's coefficients for the bed and ice, respectively; and $\beta = \chi_i/\chi_b$.

The range of Manning's coefficients for both the river bed (n_b) and the ice cover (n_i) are also investigated. For silt and clay in the river bed of the Red River, n_b is chosen to vary from $n_b = 0.014$ to 0.046 [2]. For ice roughness, $n_i = 0.030$ varies from $n_i = 0.01$ to 0.03 [39]. Following Eq. 17, the resulted value of f_d varies from 0.011 to 0.11.



The value of λ_d has been reported to vary from $\lambda_{MC} = 0.067$ to $\lambda_{FP} = 40$ in the experiment of Shiono and Knight [43]. In the current work, λ_d is varied within the range of $\lambda_d = 0.035 - 0.1$ as reported in Pu [37].

4.3.2 Validation with field data

The parameters $(K, f_d, \text{ and } \lambda)$ are found for each cross-section I_a, I_b, I_c, I_d , and I_e separately by fitting the SKM-based solution (Eq. 16) with the field data (see section 2.3) using the ranges in section 4.3.1. From now on, the lateral (cross-stream) direction is denoted as ℓ instead of y to differentiate the field data (meandering river) from the laboratory experiment (straight channel).

As discussed in section 2, Eq. 16 requires the splitting of the cross-section into two parts: (1) the left part (outer bank); and (2) the right part (inner bank). During the fitting, the values of K and λ are selected for each cross-section while f_d is calibrated for the left and right parts independently to find f_d^l (left) and f_d^r (right).

For meandering rivers, it is not obvious how to split the cross-section appropriately because the thalweg (H_{max}) and the locations of the maximum velocity (U_d^{max}) do not coincide typically. To address this splitting issue, the separation line mid - boundary is selected in two approaches: In *Approach 1*, the mid - boundary is at the ice hole with maximum velocity (U_d^{max}) . In *Approach 2*, the mid - boundary is at the thalweg location (H_{max}) . While it is feasible to determine in advance the location of the thalweg (under

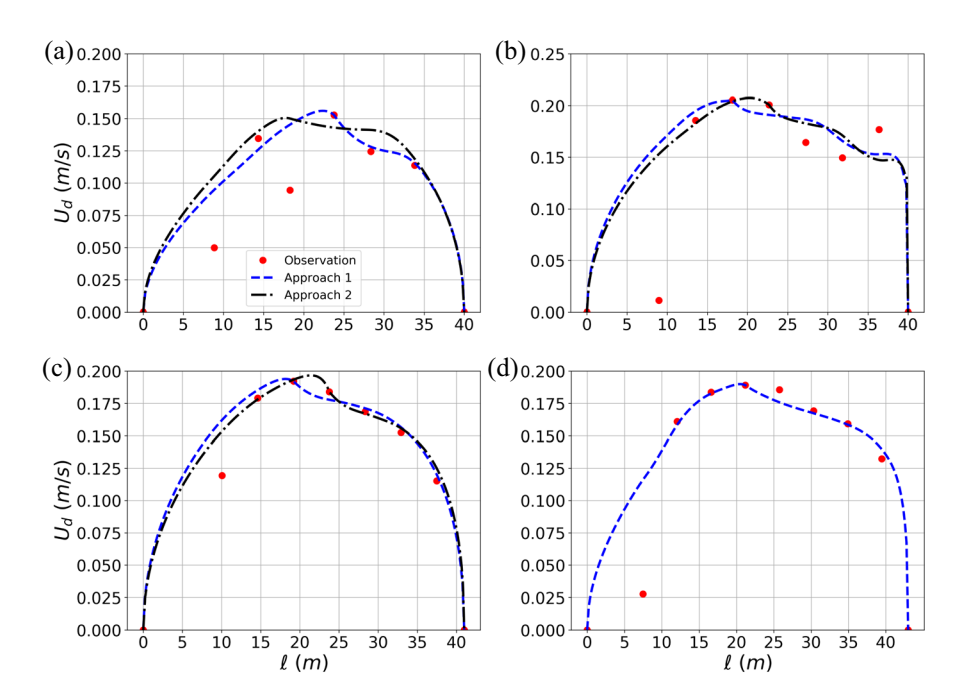


Fig. 10 The distribution of depth-averaged velocity (U_d) at cross-section **a** I_a , **b** I_b , **c** I_c , and **d** I_d . The numerical approximations (Eq. 16) are used to reconstruct U_d using two different approaches: (1) Approach 1 (maximum velocity location - blue dashed lines), and (2) Approach 2 (thalweg location - black dashed lines). The maximum velocity location coincides with the thalweg location in cross-section I_d . Therefore, a single U_d profile is shown for I_d



Table 6 Fitting parameters to estimate U_d profile using Approach 1 (the mid - boundary location at U_{max})

Section	Mid-boundary Vertical	f_d^l	f_d^r	λ_d	K
I_a	4	0.090	0.16	0.090	0.016
I_b	3	0.045	0.080	0.090	0.025
I_c	3	0.055	0.095	0.090	0.020
I_d	4	0.06	0.095	0.090	0.020
I_e	3	0.065	0.180	0.050	0.017

Table 7 Fitting parameters to estimate U_d profile using Approach 2 (the mid - boundary location is at H_{max})

Section	Mid-boundary vertical	f_d^l	f_d^r	λ_d	K
$\overline{I_a}$	3	0.095	0.120	0.09	0.016
I_b	4	0.045	0.090	0.090	0.015
I_c	4	0.055	0.110	0.090	0.020
I_d	4	0.06	0.095	0.090	0.02
I_e	5	0.065	0.300	0.050	0.010

ice-free condition, for example), it is not practical to determine the maximum velocity location before the actual ice measurement. Comparing Figs. 3 and 10, it is shown that the locations of U_d^{max} in cross-sections I_a , I_b , and I_c were slightly different ($\approx 5m$) from the locations of H_{max} (thalweg). At I_d , the locations of U_d^{max} and H_{max} coincide. Therefore, the comparison between computed values of U_d from Approach I and Approach I, and the measured depth-averaged velocity using ADCP will provide an uncertainty quantification on the estimated U_d .

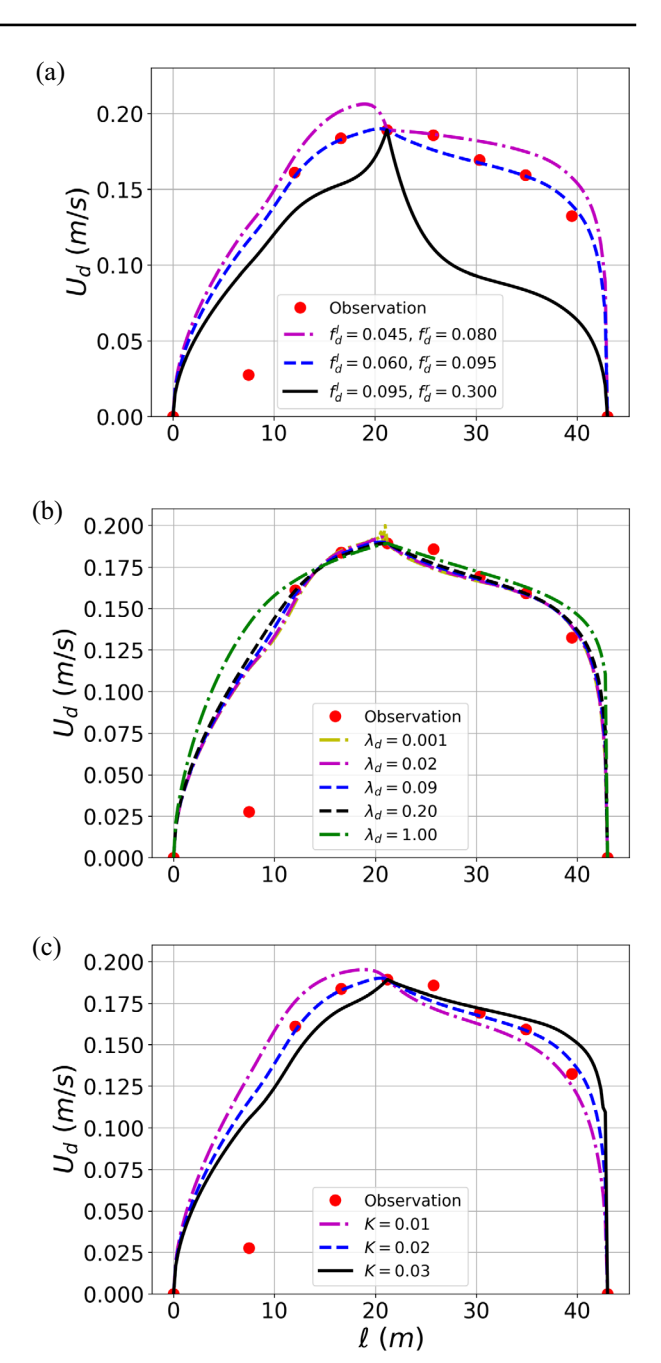
The fitted parameters for all cross-sections using Approach 1 and Approach 2 are shown in Tables 6 and 7, respectively. Comparing the results from Approach 1 and Approach 2 in Fig. 10, it is evident that the fitted profiles U_d do not depend on the choice of the mid-boundary point significantly. Comparing the obtained values of K, λ_d , f_d^r , f_d^l , it is clear that the differences are minimal between the two approaches. In short, the choice of the mid-boundary has a minimal impact on the fitted parameters as well as the obtained profile U_d .

4.3.3 Sensitivity analysis

To examine the dependence of U_d on the governing parameters (K, λ_d, f_d) , a sensitivity analysis is carried out for the cross-section I_d . Since the locations of U_{max} and H_{max} coincide at I_d , there is only one choice for the mid-boundary location. Therefore, the computed profile at I_d depends only on the values of (K, λ_d, f_d) , which are perturbed around $f_d^l = 0.06, f_d^r = 0.095, \lambda_d = 0.09, K = 0.02$ as shown in Tables 6 and 7. During the perturbation, only one parameter (either K, λ_d, f_d^l , or f_d^r) is changed whereas the others are kept unchanged as shown in Fig. 11. First, our results show that the profile U_d is most sensitive to the choice of the friction factor f_d as illustrated in Fig. 11a. This result justifies our rationale to separate the choice for f_d^l and f_d^r independently for the left and right parts of each cross-section. This separation in all cross-sections show that the friction factor of the



Fig. 11 The sensitivity of $U_d(y)$ on the variability of governing parameters: **a** the friction factors $(f_d^l \text{ and } f_d^r)$; **b** the dimensionless eddy-viscosity (λ_d) ; and **c** the secondary flow coefficient (K)



inner bank is greater than the outer-bank one. Second, the impact of the dimensionless eddy-viscosity (λ_d) is found to be relatively insignificant as seen in Fig. 11b. Although the value of λ_d is perturbed to very low and high values $(\lambda_d = 0.001$ to $\lambda_d = 1)$, the profile of U_d does not change considerably. Third, the sensitivity of the secondary flow coefficient



(K) is tested as well. Our results show that K has a relatively low impact on the depth-averaged velocity profile as seen in Fig. 11c. On the other hand, K has a significant role in determining the maximum velocity location. A low value of K coefficient tends to elevate U_d^{max} towards the outer bank. In conclusion, the friction factor plays the most important role in estimating the accurate range of U_d profile, while the secondary flow coefficient significantly impacts the maximum velocity position.

5 Discussion

5.1 Numerical procedure to compute U_d

In this study, a novel method for computing depth-averaged profile (U_d) in ice-covered streams is proposed using the Shiono-Knight method (SKM). The proposed method is validated with the laboratory data of Wang et al [53] and our results from Large Eddy Simulation as shown in Fig. 9. The method is then applied for field data [22] in a bend of the Red River of the North (United States) as depicted in Fig. 10. The results show that the proposed method is able to replicate the experimental and simulation data well. The proposed method alleviates the constraints of the analytical solutions [53], which are only available for simple cross-sections. Therefore, our method applies to alluvial channels with arbitrary cross-sections.

Our proposed method (Eq. 16) requires only the knowledge of (i) the Darcy-Weisbach friction factor (f_d) ; (ii) the dimensionless eddy viscosity (λ_d) ; and (iii) the secondary flow factor K. As shown in section 4.3.1, it is possible to estimate the range of values of f_d , λ_d , and K using physical arguments. This is in contrast to the need to calibrate C_1 , C_2 , C_3 and C_4 in the analytical solution (Eq. 6 and Eq. 8) for a specific case in which it is unclear how to determine these values using physical measurements. In short, the proposed method is fully physically-based and the fitted values of f_d , λ_d , and K can be used to interpret the hydraulic characteristics of the channel.

Our method requires the separation of one cross-section into the left and right parts and the value of U_d at the separation line (mid-boundary location). As Eq. 16 only requires boundary conditions at the beginning and end verticals, it does not dictate how to choose the mid-boundary location. While the choice of the mid-boundary location is obviously at the channel's center for symmetrical channels (see Fig. 1), it is not entirely clear how to apply the procedure for irregular cross-sections because the thalweg (H_{max}) and the location of U_{d}^{max} are not necessarily at the same place. The location of U_{max} tends to shift towards the outer bank [1] in meandering channels. Our analysis in Fig. 10 indicates that the choice of the mid-boundary location does not significantly affect the reconstructed U_d profile in the straight part of the river reach. This is important because the cross-section shape H(y) can be measured independently from the flow measurement during the opensurface condition. Therefore, the profile of U_d under ice-covered conditions can be recovered using our method with a single point of measurement at the thalweg location. This advantage will enable the fast calculation of $U_d(y)$ if the values of f_d , λ_d , and K are estimated from physical arguments [49].

Our analysis in Fig. 11 shows that f_d has the most significant impact on the $U_d(y)$ profile. As the cross-section is split into two parts, the friction factors of the left and right sections of each cross-section (f_d^l and f_d^r) are found to be slightly different from each other as shown in Tables 6 and 7 for cross-section I_a to I_d . The results show that the friction factor near



the inner bank (right) is always greater than the friction factor near the outer bank (left): $f_d^r > f_d^l$. These values of f_d agree well with the expected range in section 4.3.1. This is an unexpected finding since the measured values of U_d do not indicate a large skewness of the profile toward the outer bank. However, our method is able to reflect this trend.

5.2 The double-stacked vortices

Laboratory conditions [51] indicate that the vertical profiles can possess two points of inflections [50] in ice-covered flows. Field measurement of Demers et al [6] confirms that this feature indeed exists in a natural bend. Urroz and Ettema [51] suggests that the flow structures consist of two counter-rotating circulations in the same vertical. Field data of Lotsari et al [30] suggests that the presence of the double-stacked vortices is sensitive to the water depth. Our simulation results for the trapezoidal channel in Fig. 8 indicate that the double-stacked vortices can exist in the shallow area (floodplain). This result agrees well with the secondary flow patterns reported by Wang et al [53]. Moreover, our results indicate that the peak secondary flow is approximately 5% of the bulk velocity \overline{U} , which is consistent with the observed ranges of the coefficient K in Table 5. In addition, the secondary flow pattern suggests that the turbulent stresses are strongly correlated with the formation of the double-stack vortices in Fig. 8b, c. This is remarkable because it highlights that it is possible for the presence of high turbulent stresses near channel banks due to the interaction of these vortices with the channel's bed.

5.3 Limitation

As Eq. 16 is derived for a straight channel (see Eq. 1), it is important to test its applicability for cross-sections at meandering bends. While cross-section I_a , I_b , I_c , and I_d are at the straight section of the river reach, the cross-section I_e is at the bend apex as shown in Fig. 2. Note that the cross-section shape of I_e is rather symmetrical (the thalweg at $\ell \approx 20\,m$) as shown in Fig. 12a. The locations of U_{max} and H_{max} are separated at a distance of more than 5 m. Two approaches of fitting (Approach 1 and 2) provide significantly different profiles as seen in Fig. 12b. Moreover, both approaches cannot capture correctly the location of U_{max}^{dax} . In addition, the fitted values of f_d^r in Tables 6 and 7 are much higher than

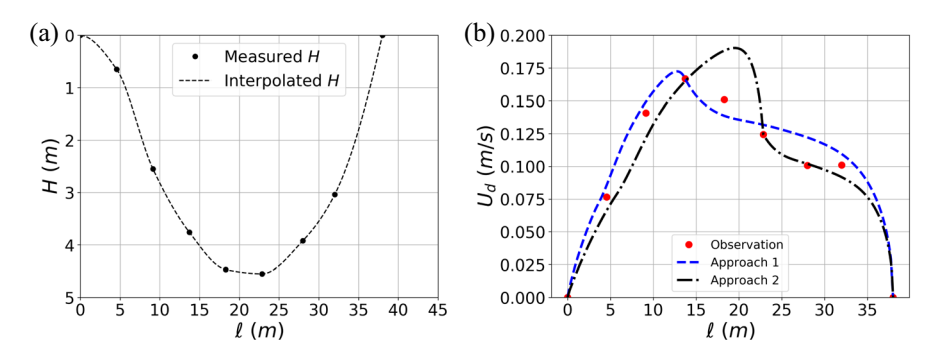


Fig. 12 a Cross-section I_e at the bend apex (see Fig. 2); and b U_d profiles based on Approach 1 and Approach 2



the expected value of 0.1. These results indicate that our method is mostly applicable to straight reaches. When it is applied for curved bends, its result might yield an unphysical shape of U_d .

6 Conclusion

A new method for computing depth-averaged profiles in ice-covered flows is proposed. The method is then validated with laboratory, numerical simulation, and field data. Our results showed that the method is applicable to natural channels with irregular cross-sections. The following conclusions are made:

- 1. The proposed method (Eq. 16) is applicable for ice-covered flows with arbitrary cross-sections. However, it is mostly suited for straight river reaches. When it is applied to river bends, it might result in inaccurate profiles.
- 2. Once the cross-section (H(y)) is known in advance, our method can provide the depth-averaged profile $(U_d(y))$ with data from a single ice hole at the thalweg location.
- Our Large Eddy Simulation results show that the double-stacked vortices might exist in ice-covered streams near both banks if the local flow depth is low. The presence of the double-stacked vortices might impact the turbulent stresses.
- 4. Our results show that the key parameters governing the U_d profile are (K, f_d, λ_d) . The value of f_d is the most important factor to determine the shape of the profile. It is possible to extract the value of f_d from field measurements, which can provide important information on the resistance of ice cover.

Acknowledgements We also acknowledge the use of computational resources at the Center for Computationally Assisted Science and Technology (CCAST)-NDSU and an allocation (CTS200012) from the Extreme Science and Engineering Discovery Environment (XSEDE), which is supported by National Science Foundation grant number ACI-1548562. We give special thanks to Dr. Xuefeng Chu (NDSU) for initiating our interest in ice hydraulics. We acknowledge the assistance of Daniel Thomas (USGS) and the Dakota Water Science Center in measuring and providing data for flows under ice coverage. We would like to thank Peter Goettsch and Christopher Broz (USGS) for helping us set up the measurement configuration.

Author contributions Berkay Koyuncu: Conceptualization, Methodology, Software, Data curation, Formal analysis, Validation, Writing - original draft, visualization; Lahcen Akerkouch: Conceptualization, Formal analysis; Trung Bao Le: Conceptualization, Methodology, Supervision, Writing - original draft, Funding acquisition. All authors reviewed the final manuscript

Funding This work is supported by the NSF CAREER No. 2239799 and a start-up package for Trung Le (North Dakota State University). Berkay Koyuncu is supported by pre-doctoral fellowships from the Environmental Conservation Sciences Program at NDSU, North Dakota Water Resources Research Institute, and the United State Geological Survey (No. 2020ND073B - Trung Le).

Data Availability LiDAR data from the State Water Commission of North Dakota are available at https://lidar.dwr.nd.gov/. Our raw velocity data are available at https://github.com/trunglendsu/ESIP/tree/main/ADCP_Data and https://github.com/trunglendsu/ESIP/tree/main/Modeling-the-shear-stress-distribution-in-a-cross-section-of-an-ice-covered-stream-main

Declarations

Conflict of interest The authors declare they have no financial interests.



Open Access This article is licensed under a Creative Commons Attribution 4.0 International License, which permits use, sharing, adaptation, distribution and reproduction in any medium or format, as long as you give appropriate credit to the original author(s) and the source, provide a link to the Creative Commons licence, and indicate if changes were made. The images or other third party material in this article are included in the article's Creative Commons licence, unless indicated otherwise in a credit line to the material. If material is not included in the article's Creative Commons licence and your intended use is not permitted by statutory regulation or exceeds the permitted use, you will need to obtain permission directly from the copyright holder. To view a copy of this licence, visit http://creativecommons.org/licenses/by/4.0/.

References

- Abad JD, Garcia MH (2009) Experiments in a high-amplitude Kinoshita meandering channel: 1.
 Implications of bend orientation on mean and turbulent flow structure. Water Resour Res 45(2):7016
- Barnes HH (1967) Roughness characteristics of natural channels. Government Printing Office, US, p 1849
- 3. Biron PM, Lane SN, Roy AG et al (1998) Sensitivity of bed shear stress estimated from vertical velocity profiles: the problem of sampling resolution. Earth Surf Process Landf J Br Geomorphol Group 23(2):133–139
- 4. Brayall M, Hicks F (2012) Applicability of 2-d modeling for forecasting ice jam flood levels in the hay river delta, Canada. Can J Civil Eng 39(6):701–712
- Calderer A, Yang X, Angelidis D et al (2015) Virtual flow simulator. Technical report, University of Minnesota, Minneapolis, MN (United States)
- Demers S, Buffin-Bélanger T, Roy A (2011) Helical cell motions in a small ice-covered Meander river reach. River Res Appl 27(9):1118–1125
- Devi K, Khatua KK (2020) Boundary shear distribution in a compound channel with differential roughness. In: Proceedings of the institution of civil engineers-water management, Thomas Telford Ltd, pp 274–292
- Devi K, Das BS, Khuntia JR et al (2021) Analytical solution for depth-averaged velocity and boundary shear in a compound channel. In: Proceedings of the institution of civil engineers-water management, Thomas Telford Ltd, pp 143–158
- Einstein HA (1942) Formulas for the transportation of bed load. Trans Am Soc Civil Eng 107(1):561–577
- Ervine DA, Babaeyan-Koopaei K, Sellin RH (2000) Two-dimensional solution for straight and meandering overbank flows. J Hydraul Eng 126(9):653–669
- 11. Ettema R (2002) Review of alluvial-channel responses to river ice. J Cold Regions Eng 16(4):191–217
- 12. Ettema R, Daly SF (2004) Sediment transport under ice. Technical report, engineer research and development center Hanover NH cold regions research
- 13. Guo J, Shan H, Xu H et al (2017) Exact solution for asymmetric turbulent channel flow with applications in ice-covered rivers. J Hydraul Eng 143(10):04017041
- 14. Kang S, Sotiropoulos F (2011) Flow phenomena and mechanisms in a field-scale experimental meandering channel with a pool-riffle sequence: insights gained via numerical simulation. J Geophys Res Earth Surf 116(F3):3011
- Kang S, Lightbody A, Hill C et al (2011) High-resolution numerical simulation of turbulence in natural waterways. Adv Water Resour 34(1):98–113
- 16. Kempema E, Reimnitz E, Clayton J Jr et al (1993) Interactions of frazil and anchor ice with sedimentary particles in a flume. Cold Reg Sci Technol 21(2):137–149
- Khosronejad A, Kang S, Sotiropoulos F (2012) Experimental and computational investigation of local scour around bridge piers. Adv Water Resour 37:73–85
- Khosronejad A, Hill C, Kang S et al (2013) Computational and experimental investigation of scour past laboratory models of stream restoration rock structures. Adv Water Resour 54:191–207
- Khosronejad A, Le T, DeWall P et al (2016) High-fidelity numerical modeling of the upper Mississippi river under extreme flood condition. Adv Water Resour 98:97–113
- Kirillin G, Leppäranta M, Terzhevik A et al (2012) Physics of seasonally ice-covered lakes: a review. Aquat Sci 74(4):659–682
- 21. Kolerski T (2014) Modeling of ice phenomena in the mouth of the vistula river. Acta Geophys 62(4):893-914
- 22. Koyuncu B, Le T (2021) Impacts of ice coverage on velocity profiles in a bend. In: AGU fall meeting abstracts, pp EP15E-1362



- Koyuncu B, Le TB (2022) On the impacts of ice cover on flow profiles in a bend. Water Resour Res 58(9):e2021WR031742
- Koyuncu B, Le TB (2024) Modeling shear stress distribution in ice-covered streams. Geological Society, London
- 25. Larsen P (1973) Hydraulic roughness of ice covers. J Hydraul Div 99(1):111–119
- Larsen PA (1969) Head losses caused by an ice cover on open channels. Boston Society of Civil Engineers, Boston
- Lau YL, Krishnappan BG (1981) Ice cover effects on stream flows and mixing. J Hydraul Div 107(10):1225–1242
- Le TB, Khosronejad A, Sotiropoulos F et al (2018) Large-eddy simulation of the mississippi river under base-flow condition: hydrodynamics of a natural diffluence-confluence region. J Hydraul Res 57:15342
- Lindenschmidt KE (2017) Rivice-a non-proprietary, open-source, one-dimensional river-ice model. Water 9(5):314
- 30. Lotsari E, Kasvi E, Kämäri M et al (2017) The effects of ice cover on flow characteristics in a subarctic meandering river. Earth Surf Proc Land 42(8):1195–1212
- 31. Lotsari E, Tarsa T, Kämäri M et al (2019) Spatial variation of flow characteristics in a subarctic meandering river in ice-covered and open-channel conditions: a 2d hydrodynamic modelling approach. Earth Surf Proc Land 44(8):1509–1529
- 32. Lotsari E, Lintunen K, Kasvi E et al (2022) The impacts of near-bed flow characteristics on river bed sediment transport under ice-covered conditions in 2016–2021. J Hydrol 615:128610
- 33. Marusic I, Monty JP, Hultmark M et al (2013) On the logarithmic region in wall turbulence. J Fluid Mech 716:R3
- Parthasarathy R, Muste M (1994) Velocity measurements in asymmetric turbulent channel flows. J Hydraul Eng 120(9):1000–1020
- 35. Petrie J, Diplas P (2016) Evaluation of the logarithmic law of the wall for river flows. River Res Appl 32(5):1082–1093
- 36. Petrie J, Diplas P, Gutierrez M et al (2013) Data evaluation for acoustic doppler current profiler measurements obtained at fixed locations in a natural river. Water Resour Res 49(2):1003–1016
- 37. Pu JH (2019) Turbulent rectangular compound open channel flow study using multi-zonal approach. Environ Fluid Mech 19(3):785–800
- 38. Shen HT (2010) Mathematical modeling of river ice processes. Cold Reg Sci Technol 62(1):3-13
- 39. Shen HT, Yapa PD (1986) Flow resistance of river ice cover. J Hydraul Eng 112(2):142–156
- Shen HT, Wang DS, Lal AW (1995) Numerical simulation of river ice processes. J Cold Reg Eng 9(3):107–118
- 41. Shen HT, Su J, Liu L (2000) SPH simulation of river ice dynamics. J Comput Phys 165(2):752-770
- Shiono K, Knight D (1988) Two-dimensional analytical solution for a compound channel. In: Proceedings of 3rd international symposium on refined flow modelling and turbulence measurements, Universal Academy Press, pp 503–510
- Shiono K, Knight DW (1991) Turbulent open-channel flows with variable depth across the channel. J Fluid Mech 222:617–646
- 44. Smith K, Cockburn JM, Villard PV (2023) Rivers under ice: evaluating simulated morphodynamics through a riffle-pool sequence. Water 15(8):1604
- Sun X, Shiono K (2009) Flow resistance of one-line emergent vegetation along the floodplain edge of a compound open channel. Adv Water Resour 32(3):430–438
- Tang X, Knight DW (2015) The lateral distribution of depth-averaged velocity in a channel flow bend.
 J Hydro Environ Res 9(4):532–541
- 47. Tatinclaux JC, Gogus M (1983) Asymmetric plane flow with application to ice jams. J Hydraul Eng 109(11):1540–1554
- Teal MJ, Ettema R, Walker JF (1994) Estimation of mean flow velocity in ice-covered channels. J Hydraul Eng 120(12):1385–1400
- Tian H, Yu M, Liu Y et al (2021) Analytical model for lateral depth-averaged velocity distributions in curved channels. In: Proceedings of the institution of civil engineers-water management, Thomas Telford Ltd, pp 99–108
- 50. Tsai WF, Ettema R (1996) A study of ice-covered flow in an alluvial bend. 376, Iowa institute of hydraulic research, college of engineering, The University
- 51. Urroz GE, Ettema R (1994) Application of two-layer hypothesis to fully developed flow in ice-covered curved channels. Can J Civ Eng 21(1):101–110
- 52. Van Balen W, Uijttewaal WS, Blanckaert K (2010) Large-eddy simulation of a curved open-channel flow over topography. Phys Fluids 22(7):075108



- Wang F, Huai W, Liu M et al (2020) Modeling depth-averaged streamwise velocity in straight trapezoidal compound channels with ice cover. J Hydrol 585:124336
- Wang F, Huai W, Guo Y (2021) Analytical model for the suspended sediment concentration in the icecovered alluvial channels. J Hydrol 597:126338
- 55. Wang F, Huai W, Guo Y et al (2021) Turbulence structure and momentum exchange in compound channel flows with shore ice covered on the floodplains. Water Resour Res 57(4):e2020WR028621
- Weiss A, Clark SP, Rennie CD et al (2015) Estimation of total suspended solids concentration from ADCP backscatter and hydraulic measurements. J Hydraul Res 53(5):670–677
- 57. Yang X, Pavelsky TM, Allen GH (2020) The past and future of global river ice. Nature 577(7788):69-73
- 58. Zhang J, Wang W, Li Z et al (2021) Analytical models of velocity, reynolds stress and turbulence intensity in ice-covered channels. Water 13(8):1107
- Zhong Y, Huai W, Chen G (2019) Analytical model for lateral depth-averaged velocity distributions in rectangular ice-covered channels. J Hydraul Eng 145(1):04018080

Publisher's Note Springer Nature remains neutral with regard to jurisdictional claims in published maps and institutional affiliations.

